Heat Flux Pattern in Detached L- and ELM Mitigated H-Modes with Rotating Magnetic Perturbations in ASDEX Upgrade

D. Brida[1, 2], T. Lunt[1], M. Wischmeier[1], M. Bernert[1], D. Carralero[1], M. Faitsch[1], Y. Feng[3], T. Sehmer[1], B. Sieglin[1], W. Suttrop[1], E. Wolfrum[1], the ASDEX Upgrade Team[1], and the MST1 Team*

[1]Max-Planck-Institut für Plasmaphysik, Boltzmannstr. 2, D-85748 Garching bei München
[2]Physik-Department E28, Technische Universtität München, Boltzmannstr. 15, D-85748 Garching bei München
[3]Max-Planck-Institut für Plasmaphysik, Wendelsteinstr. 1, D-17491 Greifswald, Germany

May 8, 2017

Abstract

For the first time divertor heat and particle fluxes in high recycling and detached deuterium L- and H-mode plasmas with rotating Magnetic Perturbations (MPs) have been measured systematically in the tokamak ASDEX Upgrade (AUG). The capability to rotate the MP field in AUG enabled us to obtain full 2D profiles of the fluxes from measurements with the divertor triple Langmuir probes. As the divertor detaches it was found that the initially non-axisymmetric heat flux becomes increasingly axisymmetric and no "burn-through" of the lobes was observed in the detached divertor in H-mode. Furthermore, the measurements were compared to simulations of the transport code EMC3-EIRENE as well as a simplified model based on field line tracing.

*See http://www.euro-fusionscipub.org/mst1

1 Introduction

A promising design for future fusion devices is the divertor tokamak. Here the magnetic field exhibits a separatrix, which constitutes the boundary between a region of closed and a region of open magnetic field lines. In the region of open field lines, also called Scrape-Off Layer (SOL), the field lines intersect with the outer divertor target on the Low Field Side (LFS) and with the inner one on the High Field Side (HFS). Energy and particles diffuse from the confinement region across the separatrix and are guided from there by parallel transport along the field lines to the targets.

If no 3D perturbations are present, tokamaks can be considered as axisymmetric. For a single null configuration under attached conditions it has been shown that the target heat flux can be characterized by the power decay length λ_q of an upstream heat flux profile and the divertor broadening factor S, which accounts for the perpendicular diffusion of heat along the divertor leg [1, 2]. Under normal operating conditions in ASDEX Upgrade (AUG) the divertor broadening factor increases with decreasing divertor temperature [3, 4].

To guarantee a sufficiently long material life time of the targets it is required to limit the steady state peak heat flux to 5–10 MW m^{-2} [5]. Therefore it is desirable to increase λ_q and S to distribute the heat flux on a larger area and decrease thereby the peak heat flux. In a toroidally symmetric tokamak the total plasma wetted area is given by [6]

$$A = 2\pi R \lambda_{int} f_x, \qquad \lambda_{int} \approx \lambda_q + 1.64S, \tag{1}$$

where λ_{int} is the *integral power decay length*, and the *integral flux expansion* f_x takes into account the magnetic flux expansion and the tilting between the target and the poloidal field [2]. For λ_q and S, their values projected to the low field side midplane along the magnetic field lines have to be used in Eq. 1. A regression analysis, which included measurements of H-mode discharges from several tokamaks, found that λ_q [mm] $\approx 0.7/B_p$ [T], where B_p is the poloidal magnetic field [7]. For the divertor spreading factor a scaling according to S [mm] $\approx P_{SOL}^{0.2}$ [MW] $B_{pol}^{-0.8}$ [T] $R^{0.7}$ [m] was found for H-mode [4], where P_{SOL} is the power crossing the separatrix and R is the major radius. Because S is generally smaller than λ_q, and λ_q is independent of R, the total wetted area scales only approximately linearly with R. This creates the necessity for high volumetric power losses, e.g. by radiation, in the edge and SOL regions of the plasma [8,9]. Such conditions are achieved in the detached regime, where after a strong reduction of the heat flux also the particle flux strongly decreases. Detachment under axisymmetric conditions has been studied extensively in experiments [10, 11] and simulations [12].

In recent years 3D Magnetic Perturbations (MPs), generated by external coils, have been the subject of active research due to their mitigating effect on Edge Localized Modes (ELMs), harmful eruptions of heat and particles from the plasma confinement region. ELM mitigation and even suppression has been achieved in several tokamaks [13, 14] for certain plasma regimes. In AUG the MP field is created by 8 lower and 8 upper saddle coils located at the LFS [15]. The field created by these coils has a non-axisymmetric magnetic field component which is perpendicular to the equilibrium flux surfaces of the unperturbed case and has a strength of $10^{-3}B_T$, where B_T is the toroidal field at the magnetic axis.

Due to their 3D nature, MPs lead to a non-axisymmetric target heat flux distribution. For attached cases it is well known that this leads to a characteristic strike line splitting, with locally higher heat fluxes than in the axisymmetric case. This is illustrated in Fig. 1 (a), where heat flux profiles at a fixed toroidal position for an axisymmetric case without MPs (MPs-off) and a 3D case with MPs (MPs-on) are shown qualitatively. The heat flux distribution under these attached conditions has been studied experimentally in detail by thermography measurements and simulations [16–18]. However, for high-recycling and detached conditions the thermography signal in AUG is dominated by Bremsstrahlung emitted from the divertor region, and the heat flux with MPs under these conditions has not been analysed so far. It is therefore currently not known if detachment occurs uniformly in the toroidal direction in AUG, or if a so called *burn through* occurs, i.e. certain regions remain attached. This is illustrated in Fig. 1 (b), where the solid line shows the qualitative heat flux distribution for a detached MP-off case and the dashed line the corresponding hypothesized MP-on heat flux exhibiting a burn through. Such a scenario might be expected if the volumetric power dissipation has a strong non-linear dependence on the temperature, with considerably lower power losses in the hot and low-density regions . If the heat flux is toroidally strongly asymmetric, measures for mitigating the local heat load, such as rotating the MP field, might become necessary. An understanding of the heat flux with MPs under high-recycling and detached conditions is therefore of highly practical importance for a future fusion device in which MPs are applied to mitigate or suppress ELMs.

Section 2 describes the heat flux measurements of L-mode density ramp discharges with MPs in AUG and compares them to simulations from the 3D transport code EMC3-EIRENE and a simplified model based on field line tracing and diffusion. Section 3 discusses the heat flux pattern for ELM-mitigated high density H-modes with MPs. Finally the results are summarized in section 4.

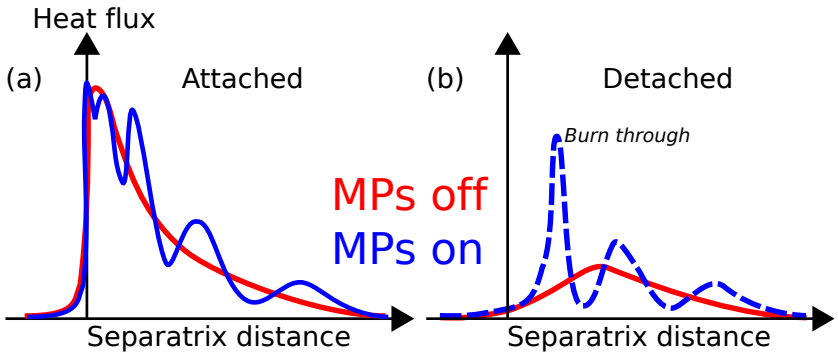

Figure 1: Illustration of hypothesized burn through effect: Qualitative heat flux profiles for attached (a) and detached (b) conditions with (on) and without (off) MPs.

2 L-Mode Deuterium Density Ramp Experiments with Rotating MPs

2.1 Experimental Setup

L-mode discharges with and without nitrogen seeding were carried out with and without MPs. Fig. 2 shows time-traces of the AUG discharge #32922 as a generic example. The toroidal magnetic field at the magnetic axis was $B_T = -2.5$ T. The plasma current and the safety factor, which are shown in Fig. 2 (a), were $I_p = 0.8$ MA and $q_{95} \approx 5.0$, respectively. This results in a ∇B_T drift directed towards the X-Point, as it is standard in AUG. The Greenwald density limit [19] for this setting is $1.0 \times 10^{20}\,\mathrm{m}^{-3}$. In Fig. 2 (b) the deuterium gas puff Φ_{D_2} can be seen. From 2.0 s on Φ_{D_2} was linearly increased from 0.35 to $20 \times 10^{21}\,e/\mathrm{s}$. The line integrated edge density n_{edge} (Fig. 2 (c)), measured along the interferometry Line-Of-Sight (LOS) H-5 [20], increases during that phase from 1.1 to $3.2 \times 10^{19}\,\mathrm{m}^{-3}$. In Fig. 2 (d) the Electron-Cyclotron-Resonance Heating (ECRH) power P_{ECRH}, the ohmic heating power P_{OH} and the total radiated power P_{radtot} measured by bolometry are plotted. Fig. 2 (e) shows the T_{div} signal, which is derived from the divertor shunt currents and serves as a proxi for the average outer target temperature [21]. In contrast to a temperature, however, this quantity can also become negative [22, 23], which indicates strong detachment.

Fig. 2 (f) shows the upper and lower MP coil currents I_{Bu1} and I_{Bl1} in sector 1. From 1.5 s on MPs with a toroidal mode number $n = 2$ in an odd configuration, i.e. with a toroidal phase difference of $\Delta\phi = -90°$ between upper and lower coil currents, were switched on. The MP field was rotated

rigidly in the toroidal direction with a rotation frequency of 5 Hz, to measure the full toroidal heat flux profile. It can therefore be ensured that the toroidal heat flux maximum at each probe position is obtained.

It should be noted that when rotating the MP field at 5 Hz its amplitude is reduced by about 50 %, compared to the static field, due to eddy currents which are induced in the passive stabilizing loop, a copper conductor located at the LFS to slow down the growth rate of the vertical displacement instability [15]. Nevertheless, such a high toroidal rotation frequency was necessary, since the plasma parameters should not change significantly during one full toroidal MP field rotation. More specifically the variation of the integrated target heat flux during one MP rotation period should be considerably smaller than the typical toroidal variations of the heat flux due to the MP field.

2.2 Heat Flux Determination by Langmuir Probe Measurements and Comparison to Thermography Data

Of particular importance for this study are divertor target heat flux measurements. The outer target is observed by an IR camera system [24] with a spatial resolution of 0.6 mm. For low densities the heat flux can be measured via this system, however, at high densities the IR signal is dominated by Bremsstrahlung emitted from the divertor region and the X-point. At these conditions the heat flux can be obtained via the flush mounted triple Langmuir probes, which have a spatial resolution of 2–3 cm. The Langmuir probes measure the electron temperature T_e and ion saturation current j_{sat} simultaneously, with a temporal resolution of 35 µs.

Since the measurement of the heat flux by the triple Langmuir probes is an indispensable technique for this study, a comparison of the data with the IR measurements at low densities was made, to asses its reliability. This section discusses briefly the physical background of energy flux measurements via Langmuir probes and describes the comparison with the IR diagnostics.

The energy flux to the target can be decomposed into the ion and electron heat flux $q_{kin,i}$ and $q_{kin,e}$, the recombination energy flux q_{rec} and reflected energy flux q_{refl}:

$$q_\perp = q_{kin,i} + q_{kin,e} + q_{rec} + q_{refl}. \tag{2}$$

The suffix $\perp$ indicates that the heat flux is perpendicular to the target surface. In the following specific expressions for the individual generic terms in Eq. 2 will be discussed. These are determined by the boundary conditions imposed by the sheath which forms in front of a target which is connected to a plasma.

At the sheath entrance the kinetic energy per ion is given by $\gamma_i T_i$, where T_i is the ion temperature and γ_i is the *ion sheath heat transmission coefficient*. Each ion is additionally accelerated by the sheath potential V_s. Therefore, the kinetic energy per ion at the target is approximately given by

$$E_0 = \gamma_i T_i + eV_s, \text{ with } V_s \approx 2.85 T_e, \tag{3}$$

for a deuterium plasma [25]. The kinetic target ion heat flux can be expressed as

$$q_{kin,i} = (\gamma_i T_i + eV_s)\Gamma, \tag{4}$$

where Γ is the ambipolar ion particle flux to the wall. Although in general, the exact value of γ_i depends on the detailed ion velocity distribution at the sheath edge, which is not known, theoretical considerations suggest that a value of $\gamma_i = 2.0$ is a reasonable assumption for a deuterium plasma [26].

However, it has to be taken into account that a fraction R_N of the ions is reflected directly from the target as neutrals. The fraction of the total kinetic ion energy which is reflected back in this process is R_E, such that the reflected energy flux can be expressed as

$$q_{refl} = -q_{kin,i} R_E. \tag{5}$$

The ion energy and particle reflection coefficients increase with decreasing ion impact energy and depend strongly on the involved elements. For example $R_E \approx 0.5$ for deuterium ions with impact energies of 20 eV impinging on a tungsten target, while for a carbon target $R_E \approx 0.1$ [27]. Therefore, it is to be expected that for a tungsten divertor target, as the one of AUG, ion reflection plays a considerably larger role than for a carbon divertor. The values used for R_E and R_N in this study are obtained from the fit function formula (6) in [27], valid for ion impact energies $E_0 < 10^5$ eV and normal ion impact angles:

$$R_{E,N} = \frac{a_1 \epsilon^{a_2}}{1 + a_3 \epsilon^{a_4}}, \quad \epsilon \equiv \frac{E_0}{\epsilon_L} \tag{6}$$

where E_0 is the impact energy given by Eq. 3, $\epsilon_L = 9.923\,26 \times 10^3$ for deuterium impinging on tungsten, and the fit coefficients $a_1, ..., a_4$ are given in table 1.

The reflection coefficients for tungsten obtained from the fit are plotted in Fig. 3 as functions of the electron temperature T_e by the red curves. For comparison the reflection coefficients for carbon are shown by the black curves. Here Eq. 3 with the assumption $T_i = T_e$ has been used.

Table 1: Fit coefficients for tungsten for the fit function Eq. 6

	a_1	a_2	a_3	a_4
R_E	2.547×10^{-1}	-1.146×10^{-1}	1.195	1.259
R_N	4.453×10^{1}	-8.079×10^{-2}	5.964×10^{-1}	1.344

The kinetic energy per electron at the sheath entrance is given by $\gamma_e T_e$, where γ_e is the *electron sheath heat transmission coefficient*. In contrast to the ions, the electrons are decelerated by the sheath potential. The kinetic target electron heat flux is therefore given by

$$q_{kin,e} = (\gamma_e T_e - eV_s)\Gamma, \tag{7}$$

with $\gamma_e = 5$. The contribution of the secondary and reflected electrons is neglected here, since it is assumed that most of these promptly return to the target surface in the presence of a shallow magnetic field angle, due to their finite Larmor radius [28].

It is further assumed that the non-reflected as well as the reflected ions recombine mainly to D_2 molecules at the target surface. The recombination energy which is deposited at the target is therefore given by

$$q_{rec} = E_{rec}\Gamma, \tag{8}$$

where E_{rec} is the sum of the ionization energy $E_{ion} = 13.6$ eV and the Franck-Condon dissociation energy per recycled ion $E_{FC,D_2} = \frac{4.5}{2}$ eV.

Inserting Eqs. 7, 5, 4 and 8 into Eq. 2 with $T = T_e = T_i$, the following expression for the target heat flux is obtained (see also [25]):

$$q_\perp = (\gamma T + E_{rec})\,\Gamma, \tag{9}$$

where

$$\gamma = \left(\gamma_i(1 - R_E) + \gamma_e - R_E\frac{eV_s}{T}\right). \tag{10}$$

Eq. 9 depends only on the quantities T_e and Γ, measured by the Langmuir probes. Inserting the numerical values for γ_i, γ_e and V_s cited above, we get $\gamma = (4.85(1 - R_E) + 2.15)$.

In Fig. 4 the outer target heat flux $q_{\perp,IR}$ of the discharge #32921, obtained by the IR diagnostics, is compared to the one obtained from the Langmuir probe measurements, according to Eq. 9. The variable Δs in Fig. 4 is the distance from the separatrix, where $\Delta s < 0$ corresponds to the private flux region and $\Delta s > 0$ to the SOL. The shown time range is $t = 2.0 \pm 0.2$ s, where the density is still low and the contribution of Bremsstrahlung to the

IR signal can consequently be neglected. In this time range the strike line is moving by about 1.5 cm. Therefore each Langmuir probe measures effectively a continuous part of the profile within these 1.5 cm. The Langmuir probe heat flux is shown once with the fitted reflection coefficients (blue) and once with $R_E = R_N = 0$ (green). As can be seen the heat flux measured by IR is overestimated by about 50 % if the ion reflection is neglected, while a considerably better agreement is obtained if reflection is taken into account.

2.3 Divertor Heat Fluxes

Figure 5 (a) shows the line integrated edge density time traces of the L-mode density ramps #32921 (MP-off, red) and #32922 (MP-on, blue). The corresponding time traces of the heat flux measurements of four adjacent Langmuir probes at the outer divertor can be seen in Fig. 5 (b-e). For the MP-off as well as the MP-on case it is found that the triple Langmuir probe temperature measurements become unreliable as the temperature drops below 5 eV. The reason of the erroneous temperature measurements might be the decreasing electron mean free path as the temperature decreases [29,30]. This leads to a decrease of the electron saturation current j^e_{sat} and the assumption that $j^e_{sat} \gg j_{sat}$, under which the temperature is derived from the triple probe measurements, is not fulfilled anymore. The triple probes can then yield unphysically high values for T_e [31]. The time ranges where the measured temperature is believed to be unreliable are indicated by the gray shaded regions in Fig. 5 (b-e).

However, for low temperatures Eq. 9 is dominated by q_{rec} and the heat flux does not depend strongly on the temperature. We can therefore assume a constant temperature in the gray shaded regions in Fig. 5 without introducing a larger error. Here the choice $T_e = 2.5$ eV was made, which is suggested by the divertor temperature derived from the shunt currents for $t > 3.0$ s (Fig. 2 (e)). At the end of this section it will be argued that the assumption of a constant T_e does not affect the results strongly.

Before discussing the MP-on case, the characteristics of the MP-off case will be briefly described. A detailed discussion of detachment in this kind of discharges at AUG can be found in [32]. Before 2.6 s the strike line position is not stationary, explaining the decrease and subsequent increase of the heat flux in Fig. 5 (b). From 2.6 s on the divertor detaches near the strike line and the heat flux decreases. As the density is increased further, detachment extends outwards and from 3.2 s on the heat flux is decreasing at all probe positions.

In the MP-on case the same trends as for the MP-off case can be seen, but with an additional oscillatory modulation of the heat flux due to the

rotating lobes that pass the probe positions. While at the strike line these oscillations are small, they become more pronounced towards the far SOL. As the heat flux decreases, the oscillation amplitude decreases as well at all probe locations. The running mean heat fluxes in the MP-on case $\left\langle q^{on}_{\perp,LP}\right\rangle$, with an averaging interval of one MP period (i.e. 0.2 s) are shown by the blue dashed lines. These follow closely the MP-off heat fluxes, showing that the MPs do not significantly affect the time averaged values.

The oscillatory nature of the heat fluxes can be seen even more clearly in Fig. 6 (b-e), where the relative deviation δ_q from the mean value is plotted. Here δ_q is defined as

$$\delta_q \equiv \frac{q^{on}_{\perp,LP} - \left\langle q^{on}_{\perp,LP}\right\rangle}{\left\langle q^{on}_{\perp,LP}\right\rangle} \tag{11}$$

Fig. 6 (a) shows the line integrated edge density of the MP-off case (#32921) and Fig. 6 (f) the upper MP coil current I_{Bu1} in sector 1. We concentrate from now on on the time period $t > 3.0$ s, where clear oscillations can be seen and the averaged heat fluxes change on a slow time scale compared to the MP period. δ_q varies strongest at the position of the outermost probe, with amplitudes as large as about 50% around 3.0 s. Furthermore, δ_q tapers off at all four probe locations as the density increases, and the largest amplitudes observed towards the end of the discharge are around 20 %. In other words the oscillation amplitude decreases faster than the average heat flux.

It should be kept in mind that a constant temperature of $T_e = 2.5$ eV was assumed in the calculation of δ_q, and therefore the oscillation of the temperature was not taken into account. From Eq. 9 we can estimate the error introduced by this assumption as

$$\Delta\delta_q = \frac{\gamma\tilde{T}_e}{\gamma T_e + E_{rec}}, \tag{12}$$

Here $\tilde{T}_e$ is the amplitude of the temperature oscillations, which we can estimate from the variations of the T_{div} signal as $\tilde{T}_e \approx 0.5$ eV. At $T_e = 2.5$ eV, $R_E = 0.55$ (see. Fig. 3) and we get $\gamma \approx 4.4$. We obtain therefore $\Delta\delta_q \approx 10$ %, which is considerably lower than the largest heat flux amplitudes of 50 % observed.

2.4 Comparison of the L-Mode Density Ramp Experiments to EMC3-EIRENE Simulations

To interpret the results presented in the last section two time points of the discharges #32921 and #32922 were simulated with the 3D transport code

EMC3-EIRENE [33]. In addition a MP-off and a MP-on time point of the low density L-mode discharge #32217, which is discussed in detail in [34], were simulated.

The code EMC3-EIRENE couples the plasma fluid transport code EMC3 with the neutral code EIRENE. Since EMC3 as well as EIRENE apply a Monte-Carlo technique to solve the underlying equations the simulation grid is not required to be flux surface aligned, enabling it to simulate the 3D plasma transport in the complex field configuration created by the MPs. As such it has become a widely used tool to study the transport in tokamaks with 3D field geometries [18, 35] and was already applied to simulate AUG discharges with MPs [16]. It should be noted that EMC3-EIRENE does not include drifts and recombination processes. Volume recombination becomes important for plasma target temperatures below about 2 eV.

The magnetic field used to construct the grid can be decomposed according to

$$\vec{B}_{tot} = \vec{B}_{eq} + \vec{B}_{MP} + \vec{B}_{resp}, \tag{13}$$

where $\vec{B}_{eq}$ is the equilibrium field without MPs, $\vec{B}_{MP}$ the vacuum field created by the coils and $\vec{B}_{resp}$ the field created by the plasma in response to $\vec{B}_{MP}$. Although it would be possible to obtain $\vec{B}_{resp}$ from magnetohydrodynamic modelling [36], for this study a simplified model was used to calculate $\vec{B}_{resp}$, which assumes that $\vec{B}_{MP}$ is ideally screened on rational surfaces [37]. This approach has already been successfully applied in EMC3-EIRENE simulations of AUG L-mode discharges with MPs [38]. The number and radial position of the screening surfaces is an ad-hoc parameter in the model. For this study all resonant rational surfaces within $\psi_N < 0.97$ were screened.

Before simulating the MP-on cases, the MP-off simulations corresponding to #32217 at 2.4 s (low density), #32921 at 3.1 s (medium density), and #32921 at 4.1 s (high density) were carried out. In Fig. 7 the simulated heat (top) and particle flux (bottom) profiles are shown for the low (a), medium (b), and high density (c) case. The corresponding probe measurements are shown by the black symbols. For the low density case, the heat flux could also be measured by the infrared system, shown by the green curve.

The simulation input parameters were chosen such that a satisfactory agreement with the heat flux measurements was obtained. The respective net input powers and recycling fluxes were $P_{net} = 0.25$ MW and $\Phi_r = 5.0 \times 10^{21}\, e/\mathrm{s}$ for the low density, $P_{net} = 0.5$ MW and $\Phi_r = 6.6 \times 10^{22}\, e/\mathrm{s}$ for the medium density, and $P_{net} = 0.4$ MW and $\Phi_r = 4.0 \times 10^{22}\, e/\mathrm{s}$ for the high density case. The diffusion coefficients for particles $D_\perp$ and ion and electron heat $\chi_{i,\perp}$ and $\chi_{e,\perp}$ are ad-hoc parameters in EMC3-EIRENE. They were adapted individually for each simulated time point.

For the low density case, a good agreement of the simulation results with the measured heat flux was achieved, while the saturation current j_{sat} is underestimated by about a factor of two in the far SOL. For the medium density case both, heat and particle flux profiles, are in good agreement with the measured data. For the high density case, the heat as well as the particle flux distributions are centered closer to the separatrix than the measurement results. This might be a consequence of the lack of volume recombination in the code, leading to an overestimation of the particle flux near the strike line and consequently also of the heat flux. However, the magnitude of the heat as well as the particle flux are approximately in agreement with $q_{LP,\perp}$ and j_{sat}, respectively.

The simulations for the MP-off cases were repeated with MPs, i.e. with the field given by Eq. 13, while the input parameters were kept constant. Fig. 8 (a) shows the corresponding simulated heat flux profiles (blue) for #32217 at the toroidal angle $\phi = 40°$. The green curve shows the heat flux obtained by thermography in #32217 at 5.0 s, where the MPs were switched on. In Fig. 8 (b) and (c) the simulated heat flux profiles of #32922 at 3.1 s and 4.1 s at the toroidal angles $\phi = 40°$ (solid, blue) and $\phi = 130°$ (dashed, blue) are shown. The black symbols show the corresponding heat flux measured by the Langmuir probes. The error bar of the probe measurements in Fig. 8 (b) and (c) indicate the amplitude of the toroidal heat flux variation, which is defined as

$$\Delta q_\perp \equiv \sqrt{2}\sigma_q \tag{14}$$

Here σ_q is the standard deviation over one MP period of $q_\perp$. The signal processing procedure to obtain σ_q is depicted in Fig. 9 for the heat flux obtained by an outer target triple Langmuir probe in the H-mode deuterium discharge #33226, which will be discussed in more detail in section 3. A median filter was applied here to the data to remove outliers, e.g. due to the small ELMs. The unfiltered data is shown in green and the median filtered data in blue. In red the average value $\langle q_{\perp,LP} \rangle$ and the amplitude $\Delta q_{\perp,LP}$ over one MP period around 3.75 s are shown. For the L-mode case discussed here an arithmetic mean filter was applied instead of a median filter.

It can be seen in Fig. 8 that the toroidal heat flux variations show the same tendency in the simulations as observed in the experiment: the lobes in the heat flux distribution smooth out and it becomes increasingly axisymmetric as the heat flux decreases.

It is illustrative to compare the simulated MP-on target heat flux results to a semi-analytical model, similar to the ones presented in Refs. [39, 40], which is described in the following. For this it is helpful to bear in mind that in an unperturbed plasma energy is transported from the core region to the

SOL by cross-field diffusion, where it can be transported along the field lines to the target. The competition between parallel and perpendicular heat conduction in the SOL results in an exponential decay of the parallel heat flux with the e-folding length λ_q. However, In a magnetically perturbed plasma no clear SOL is defined, since field lines can perform multiple poloidal turns before hitting the other target and connection lengths within a broad spectrum exist. The model assumes, similar to the unperturbed SOL, that the parallel heat flux along a field line is dominated by the cross field diffusion along its last poloidal turn. Furthermore it is assumed that the resulting parallel heat flux depends exponentially on the minimum unperturbed poloidal flux ψ_{min} reached during that last poloidal turn. The parallel heat flux along a field line hitting the outer target at the separatrix distance Δs and the toroidal angle ϕ is then given by

$$q_{\parallel}^{u,on}\left(\Delta s, \phi\right) = q_0^{on} e^{-\frac{r_{min}}{\lambda_q^{on}}} \tag{15}$$

where r_{min} is the outboard midplane position corresponding to the ψ_{min} of that field line. q_0^{on} is a normalization constant and λ_q^{on} is the power decay length. The superscript *on* is used to discriminate the quantities from the respective MP-off values. ψ_{min} was obtained by numerical field line tracing. The MP field used in the field line tracing was the same as in the simulations, i.e. screening was included.

The diffusion along the divertor leg is, as in the 2D case, taken into account by a convolution with a Gaussian of width S^{on} [1, 7]. That is the target heat flux is given by

$$q_{\parallel} = q_{\parallel}^{u,on}\left(\Delta s, \phi^t\right) \otimes \frac{1}{f_x S\sqrt{\pi}} \exp\left(\frac{-\Delta s^2}{\left(f_x S^{on}\right)^2}\right), \tag{16}$$

where the factor $f_x \approx 4.5$ is the integral flux expansion. The symbol $\otimes$ represents the convolution.

The 1D profiles obtained by the model are shown in Fig. 8 (a-c) by the red curves. For the profiles shown in Fig. 8 (b) and (c) a satisfactory agreement between the model and the EMC3-EIRENE simulations was found by choosing $\lambda_q^{on} = \lambda_q^{off}$ and $S^{on} = S^{off}$. Here λ_q^{off} and S^{off} were obtained by fitting Eq. 2 from [2] to the MP-off solution. For the low density profile shown in Fig. 8 (a), a higher divertor spreading factor than in the MP-off case, with $S^{on} = 1.4 S^{off}$, had to be chosen to obtain agreement between the EMC3-EIRENE simulation and the model.

In Fig. 10 (top) the full simulated 2D outer divertor target heat flux patterns for the low density (left) and the high density case (right), and the corresponding heat flux pattern obtained by the model (bottom) are shown.

To highlight the effect of the divertor spreading factor S, in Fig. 10 (middle) the corresponding patterns with the assumption of no divertor spreading (i.e. $S^{on} = 0$) are shown. Here for both cases a strong non-axisymmetry with distinct lobe structures can be observed. For the high density case S^{on} is about 15 times larger than for the low density case. Hence the the smearing out of the lobes is considerably stronger for the higher density. For attached L-mode plasmas this smearing out effect of the lobes with increasing S has already been shown experimentally in ASDEX Upgrade [34,40]. Futhermore, in Ref. [40] the experimental results could be reproduced with a similar model to the one used here.

3 ELM-mitigated High Density Deuterium H-Mode Experiments with Nitrogen Seeding and Rotating MPs

In the last section it was shown that for typical L-mode conditions no burn through occurs. However, as discussed in section 1, MPs are considered as an option to mitigate or suppress ELMs in H-mode discharges in future fusion devices, such as ITER. For these conditions the transport properties differ from L-mode and the results presented in the last section are not automatically transferable. To measure the fluxes with MPs under these conditions a comprehensive set of H-mode deuterium discharges, with partially ELM-mitigated conditions, were carried out in AUG. The discharges were, however, carried out at a higher collisionality than the one envisaged for ITER, since in current tokamaks a low collisionality is incompatible with the high edge densities required to reach detachment.

The typical setup for these discharges can be seen in Fig. 11, where time-traces for the discharge #33226 are shown. The shaded regions indicate the time periods where the MPs with a differential phase difference of $\Delta\phi = 180°$ were switched on. Compared to the L-mode density ramp discharge, a low MP rigid rotation frequency of 2 Hz could be used, since the H-mode discharges are stationary over several seconds. The lower rotation frequency has the advantage that the screening of the MP field by the PSL is smaller. Fig. 11 (a) shows the heating power, (b) the MP coil currents, (c) the core and edge line integrated densities n_{core} and n_{edge}, (d) the nitrogen and deuterium seeding levels Φ_{N2} and Φ_{D2} and (e) the outer divertor shunt current signal $I_{polsola}$, which serves as an ELM indicator. The toroidal magnetic field was $B_T = -2.5$ T and the plasma current $I_p = 0.6$ MA. The relatively low I_p results in a high $q_{95} \approx 6.5$ and a large λ_q [2].

The NBI heating power was constant, with $P_{NBI} = 7.5$ MW. In addition constant central ECRH heating of $P_{ECRH} = 1.25$ MW was applied during the discharge. At 5.0 s the nitrogen seeding level was raised to increase the divertor radiation and decrease the target heat flux. During the stationary phases of the discharge several MP rotations were carried out to measure the 2D divertor fluxes with the triple Langmuir probes. As can be seen in the $I_{polsola}$ signal type I ELMs were suppressed for $t \geq 2.2$ s and only small ELM-like events were observed. Note that, although ELM mitigation with MPs has been achieved before in AUG [14], in the shown discharge the type I ELMs are already suppressed before the MPs are switched on. The ELM mitigation might in this case be a result of the nitrogen seeding [41]. Also in the other H-mode discharges with nitrogen seeding and MPs carried out for this study the ELMs were already mitigated before the MP phase. Based on the $I_{polsola}$ signal, no clear effect of the MPs on the already mitigated ELM characteristics was observed.

The other discharges carried out for this study differed in the neutral beam heating P_{NBI} and/or the nitrogen seeding level Φ_{N2}. By this a scan of all relevant detachment states was achieved. Fig. 12 (a) shows the heat flux obtained by the Langmuir probes for increasingly detached states from left to right. In contrast to the L-mode discharges discussed above, the temperature obtained by the Langmuir probes was reliable in these discharges, and therefore no assumptions about the temperature had to be made. The time slices were taken from ELM-mitigated phases of the discharges #33226 and #33227 with $P_{NBI} \approx 7.5$ MW and #33228 with $P_{NBI} \approx 5.0$ MW. Fig. 12 (b) shows the MP coil current signal B_{u1}, Fig. 12 (c) the respective nitrogen and deuterium seeding levels Φ_{N2} and Φ_{D2} and Fig. 12 (d) the T_{div} signal. For the highly attached case clear oscillations of the heat flux are observed. As the nitrogen seeding is increased the heat flux decreases, however, distinct lobe structures can still be observed. For the partially detached case the lobe structures become less pronounced and no clear lobe structures are visible for the strongly detached case.

The toroidally averaged values and oscillation amplitudes of each of the 2D profiles shown in Fig. 12 (a) can be represented as 1D profiles, as already done for the L-mode discharge #32922. The resulting profiles for the different detachment states are shown in Fig. 13 by the red error bars. For comparison the corresponding MP-off profiles are shown in blue. As already observed in the 2D representation in Fig. 12 (a), the oscillations become gradually smaller as the divertor detaches. For the attached case, shown in Fig. 13 (a), the heat flux variation is around 35 %. In the pre-detached (b) and the partially detached (c) case the maximum observed relative oscillation amplitudes are 25% and for completely detached conditions (d) the relative

amplitude drops to 15%. As in the L-mode discharge, no burn through was observed for this scenario, i.e. no toroidally localized heat flux distribution was measured and the outer divertor detaches uniformly.

From the probe measurements it was found that in all cases the relative temperature oscillation amplitude $\tilde{T}_e/T_e$ is of the same magnitude as the relative particle flux oscillation amplitude $\tilde{\Gamma}/\Gamma$,. By assuming that $\gamma T_e \gg E_{rec}$ in Eq. 9, which is valid if T_e is over several eV, the relative heat flux oscillation amplitude can be expressed as

$$\delta_q \approx \frac{\tilde{T}_e}{T_e} + \frac{\tilde{\Gamma}}{\Gamma}. \tag{17}$$

Since $\tilde{T}_e/T_e \approx \tilde{\Gamma}/\Gamma$ temperature and particle flux oscillations contribute to the same amount to the heat flux oscillations.

As for the L-mode case, the heat flux profiles were fitted using the model described in section 2.4. The fitted heat fluxes are shown by the red shaded curves in Fig. 13. The vertical width of the shaded regions indicates the amplitude of the heat flux variation obtained by the fit. The power decay length λ_q used in the model was the same for each profile, with $\lambda_q = 6.8$ mm. This is about a factor two higher than the λ_q predicted by the scaling given in Ref. [2]. However, the scaling in Ref. [2] is only valid for inter-ELM regimes, while in the discharges considered here small ELMs are still present, which could effectively increase λ_q. The divertor spreading factor S used in the fit was increased and q_0 decreased for increasingly detached states. For the attached and pre-detached case a satisfactory agreement between the model and the measurements at the probe locations was achieved. However, due to their limited spatial resolution the probes do not capture the region where the modeled heat flux peaks, and no conclusions about the agreement in this region can be made. For the partially and completely detached cases it was not possible to fit the data points in the detached region near the separatrix and the data points in the far SOL simultaneously. However, in the far SOL the model still describes the measurements and the decrease of the toroidal variation may be considered as a result of perpendicular diffusion.

4 Conclusions

A comprehensive set of deuterium L- and ELM-mitigated H-mode discharges with and without MPs was carried out at AUG to study divertor conditions with MPs at high densities up to the detached regime. By rotating the MP field, the full 2D heat and particle fluxes could be measured with triple Langmuir probes. In the attached case toroidal heat flux variations of up to 50 %

were observed [34]. For partially detached and strongly detached conditions these variations decrease to below 20% and in particular no burn through was observed. For the L-mode density ramp discharges two time points were compared to simulations of the 3D transport code EMC3-EIRENE. Although, the simulations are not valid in the detached regions, where atomic processes not taken into account in EMC3-EIRENE play a role, the decrease of the toroidal heat flux variations could be reproduced. Moreover, from the EMC3-EIRENE heat fluxes without MPs the corresponding simulated heat fluxes with MPs could be obtained in good approximation by using a semi-analytical model. In the EMC3-EIRENE simulations as well as the model the decrease of the toroidal heat flux variations can be attributed to a decreasing ratio of parallel to perpendicular heat diffusion. This means that the relative effect of the perpendicular diffusion becomes larger and the heat flux variations smear out.

5 Acknowledgements

This work has been carried out within the framework of the EUROfusion Consortium and has received funding from the Euratom research and training programme 2014-2018 under grant agreement No 633053. The views and opinions expressed herein do not necessarily reflect those of the European Commission

References

[1] F. Wagner. *Nucl. Fusion*, 25(5):525, 1985.

[2] T. Eich et al. *Phys. Rev. Lett.*, 107:215001, 2011.

[3] B. Sieglin et al. *Plasma Phys. Control. Fusion*, 58(5):055015, 2016.

[4] A. Scarabosio et al. *J. Nucl. Mater.*, 463:49–54, 2015.

[5] R. P. Wenninger et al. *Nucl. Fusion*, 54(11):114003, 2014.

[6] M. A. Makowski et al. *Phys. Plasmas*, 19(5):056122, 2012.

[7] T. Eich et al. *Nucl. Fusion*, 53(9):093031, 2013.

[8] M. Wischmeier et al. *J. Nucl. Mater.*, 463:22 – 29, 2015.

[9] G. Federici et al. *Fusion Eng. Des.*, 89(7):882–889, 2014.

[10] A. Kallenbach et al. *Nucl. Fusion*, 55(5):053026, 2015.

[11] A. Loarte et al. *Nucl. Fusion*, 38(3):331, 1998.

[12] F. Reimold et al. *Nucl. Fusion*, 55(3):033004, 2015.

[13] T. E. Evans et al. *Nucl. Fusion*, 48(2):024002, 2008.

[14] W. Suttrop et al. *Phys. Rev. Lett.*, 106:225004, 2011.

[15] W. Suttrop et al. *Fusion Eng. Des.*, 84(2):290–294, 2009.

[16] T. Lunt et al. *Nucl. Fusion*, 52(5):054013, 2012.

[17] H. Frerichs et al. *Nucl. Fusion*, 50(3):034004, 2010.

[18] O. Schmitz et al. *Plasma Phys. Control. Fusion*, 50(12):124029, 2008.

[19] M. Greenwald et al. *Nuclear Fusion*, 28(12):2199, 1988.

[20] M T Bernert et al. *Plasma Physics and Controlled Fusion*, 57(1):014038, 2014.

[21] A. Kallenbach et al. *Plasma Phys. Control. Fusion*, 52(5):055002, 2010.

[22] GM Staebler and FL Hinton. *Nuclear fusion*, 29(10):1820, 1989.

[23] A Kallenbach et al. *Journal of nuclear materials*, 290:639–643, 2001.

[24] B. Sieglin et al. *Rev. Sci. Instrum.*, 86(11):113502, 2015.

[25] P. C. Stangeby et al. *The Plasma Boundary of Magnetic Fusion Devices*, volume 224. Institute of Physics Publishing Bristol, 2000.

[26] P. C. Stangeby. The plasma sheath. In *Physics of Plasma-Wall Interactions in Controlled Fusion*, pages 41–97. Springer, 1986.

[27] W Eckstein. IPP Report 17/12, 2009.

[28] D. Tskhakaya and S. Kuhn. *Contrib. Plasma Phys.*, 40(3-4):484–490, 2000.

[29] P. C. Stangeby and G. M. McCracken. *Nucl. Fusion*, 30(7):1225, 1990.

[30] J. A. Tagle et al. *Plasma Phys. Control. Fusion*, 29(3):297, 1987.

[31] R. D. Monk et al. *J. Nucl. Mater.*, 241:396–401, 1997.

[32] S. Potzel et al. *Nucl. Fusion*, 54(1):013001, 2014.

[33] Y. Feng. *Contrib. Plasma Phys.*, 44(1-3):25–30, 2004.

[34] M. Faitsch et al. 2D Heat Flux in ASDEX Upgrade L-Mode with Magnetic Perturbations.

[35] D. Harting et al. *Contrib. Plasma Phys.*, 48(1-3):99–105, 2008.

[36] F. Orain et al. *Phys. Plasmas*, 20(10):102510, 2013.

[37] P. Cahyna et al. *J. Nucl. Mater.*, 415(1):S927–S931, 2011.

[38] D. Brida et al. Determination of the Stochastic Layer Width Properties Induced by Magnetic Perturbations via Heat Pulse Experiments at ASDEX Upgrade.

[39] P. Cahyna et al. *Nucl. Fusion*, 54(6):064002, 2014.

[40] M. Faitsch et al. Scrape-Off Layer Heat Transport in ASDEX Upgrade L-Mode with Magnetic Perturbation. *Plasma Phys. Control. Fusion.* Article in preparation.

[41] PA Schneider. *Plasma Physics and Controlled Fusion*, 57(1):014029, 2014.

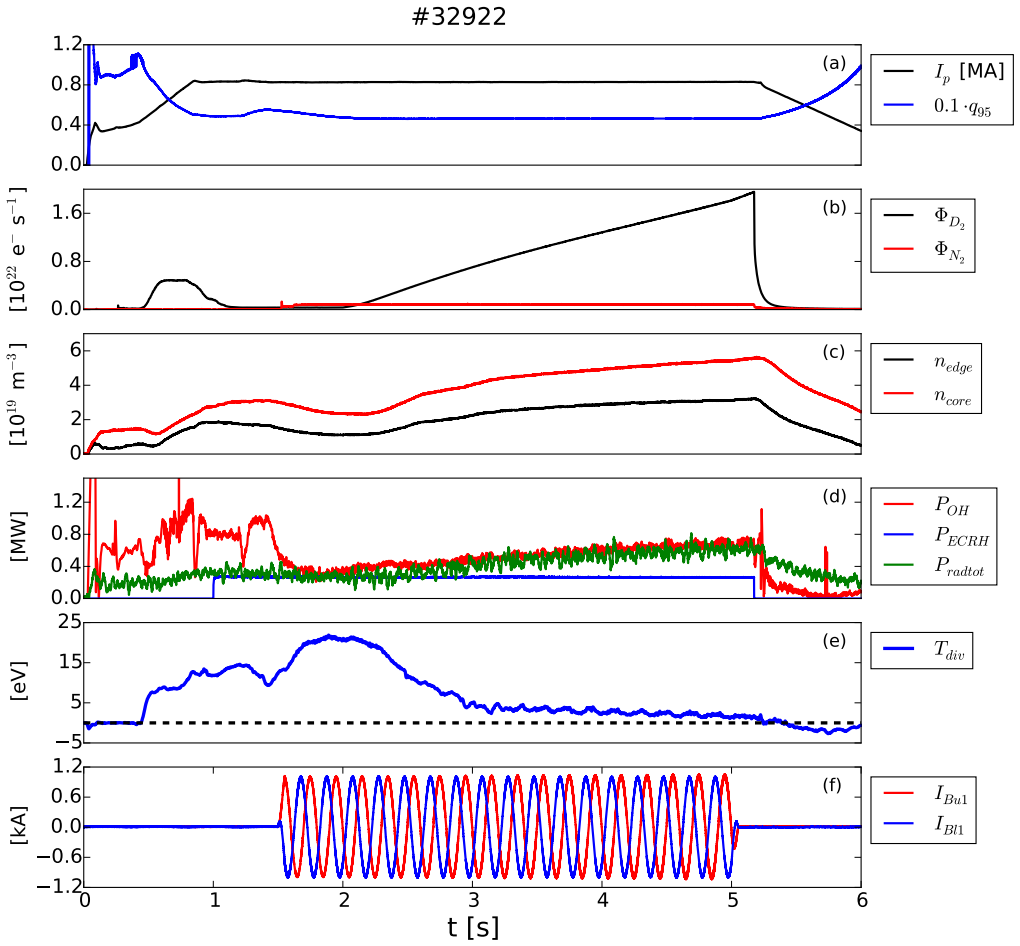

Figure 2: Time traces of plasma current I_p and safety factor q_{95} (a), deuterium and nitrogen puff rates Φ_{D2} and Φ_{N2} (b), line integrated edge and core densities n_{edge} and n_{core} (c), heating and total radiation (d), T_{div} signal derived from the divert shunt current (e), and MP coil currents I_{Bu1} and I_{Bl1} (f) for the L-mode deuterium density ramp discharge #32922.

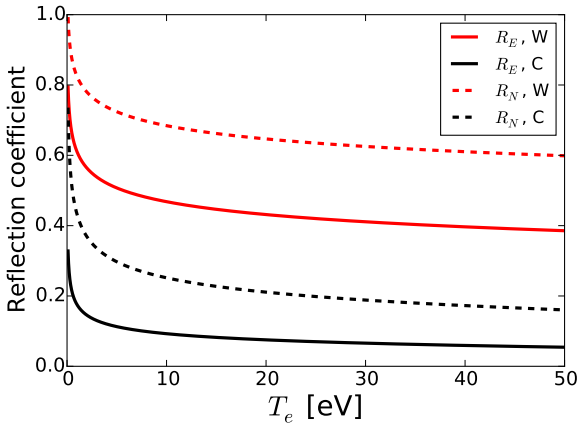

Figure 3: Energy and ion reflection coefficents R_E and R_N obtained by Eq. 6 as functions of the electron temperature T_e for tungsten (W) and carbon (C). Eq 3 and the assumption $T_e = T_i$ has been used to relate T_e to E_0.

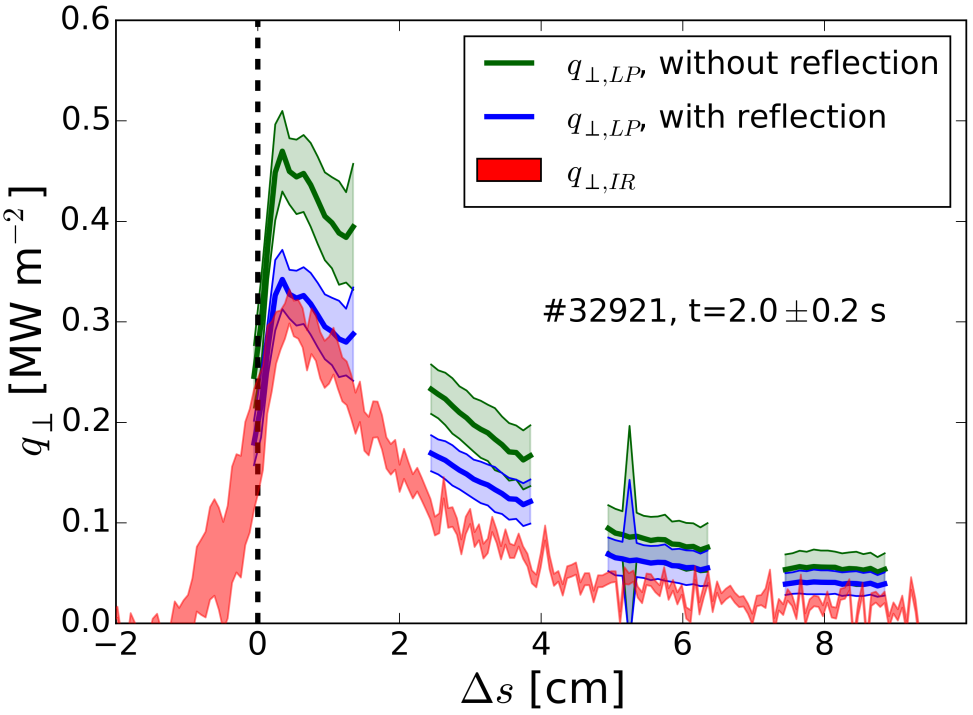

Figure 4: Thermography (red) and Langmuir probe target heat flux of discharge #32921 for the time range $t = 2.0 \pm 0.2$ s. Δs is the distance from the separatrix. The Langmuir probe heat flux is obtained via Eq. 9, once without taking ion reflection into account (green) and with reflection coefficients obtained by Eq. 6 (blue).

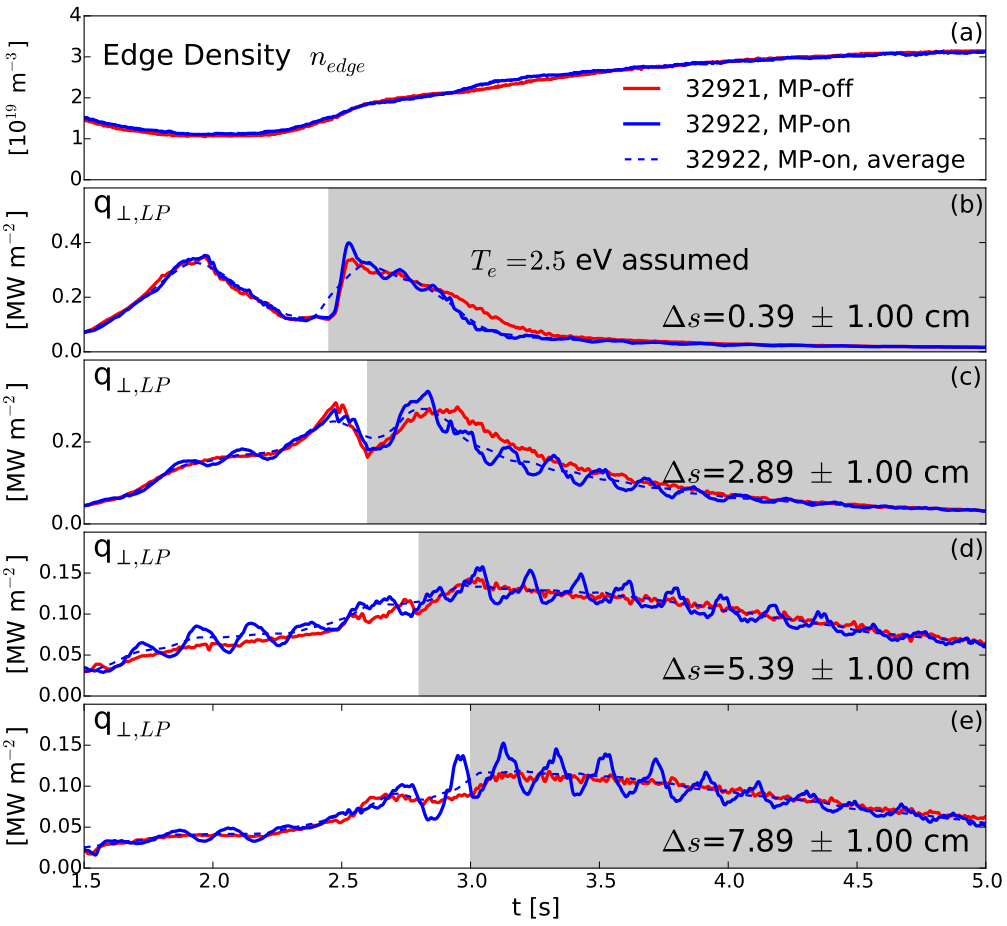

Figure 5: Line integrated edge density n_{edge} (a) and outer target heat flux obtained by triple Langmuir probe measurements at several separatrix distances Δs (b-e) for the MP-off case (red) and the MP-on case (blue). In the gray shaded regions $T_e = 2.5$ eV was assumed.

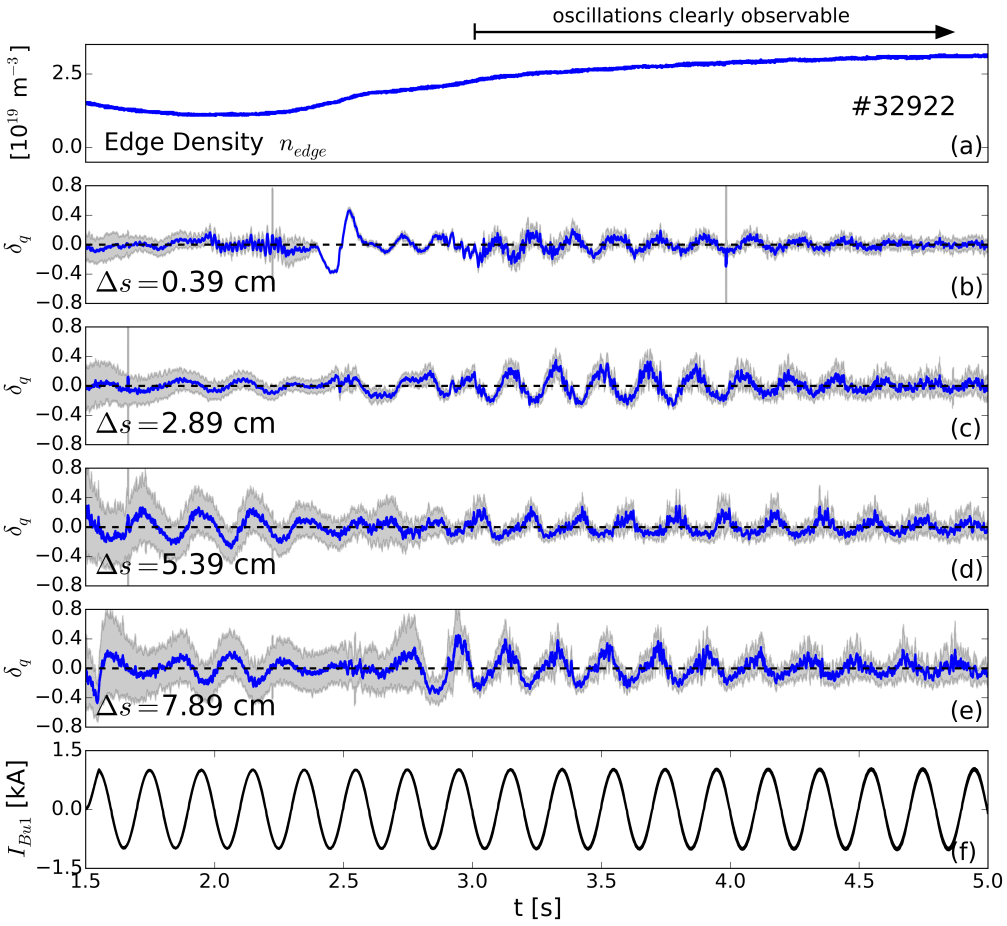

Figure 6: Line integrated edge density n_{edge} of the MP-on discharge #32922, and relative oscillations δ_q of the outer target heat flux measurements shown in Fig. 5 (b-e). In (f) the current I_{Bu1} of the upper MP coil in sector 1 is shown.

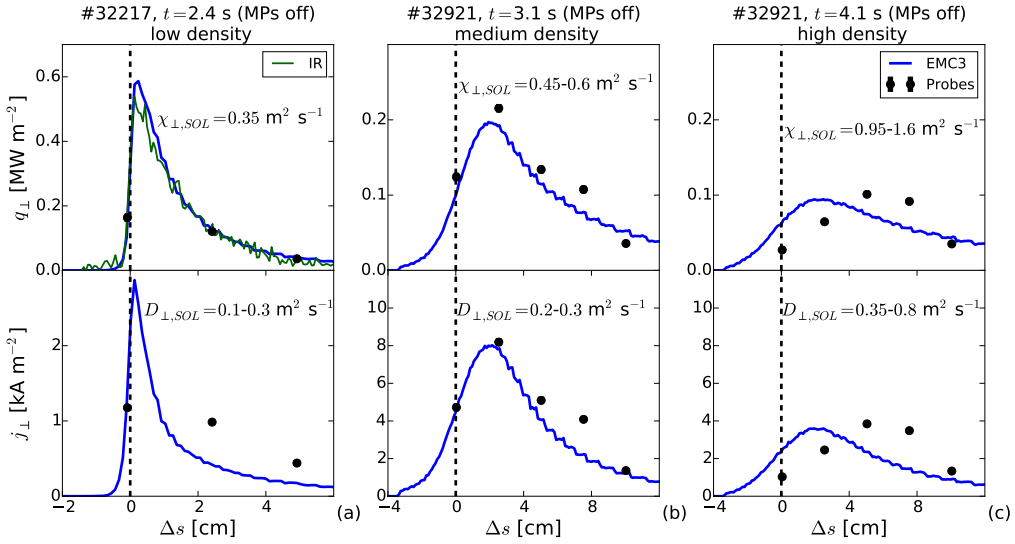

Figure 7: EMC3-EIRENE heat (top) an particle flux (bottom) simulation results for #32217, 2.4 s (a), #32921, 3.1 s (b) and #32921, 4.1 s (c).

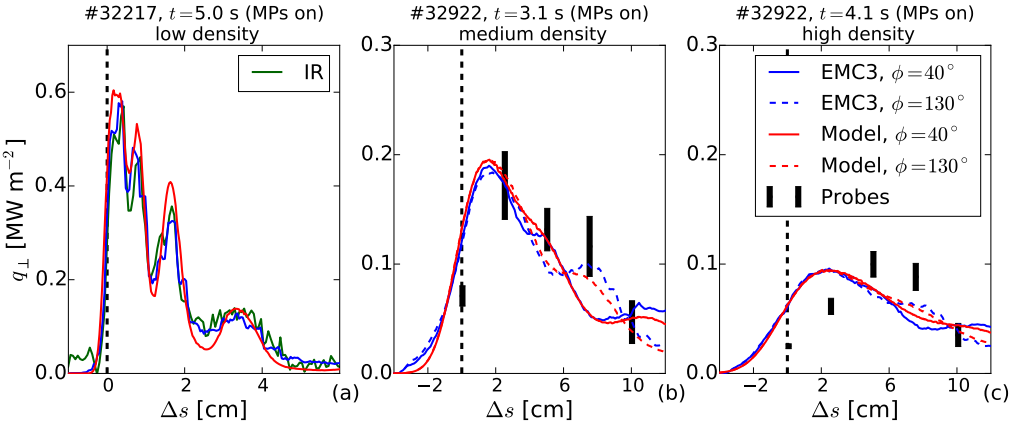

Figure 8: Comparison of the experimental heat flux profiles of #32217, 2.4 s (a), #32922, 3.1 s (b) and #32922, 4.1 s (c) with EMC3-EIRENE results (red) and ad-hoc model (blue) results at $\phi = 0°$ (solid) and $\phi = 90°$ (dashed). The green curve in (a) shows thermography measurements, and the black symbols in (b) and (c) Langmuir probe measurements. The error bars of the Langmuir probe measurements indicate the heat flux oscillation amplitude.

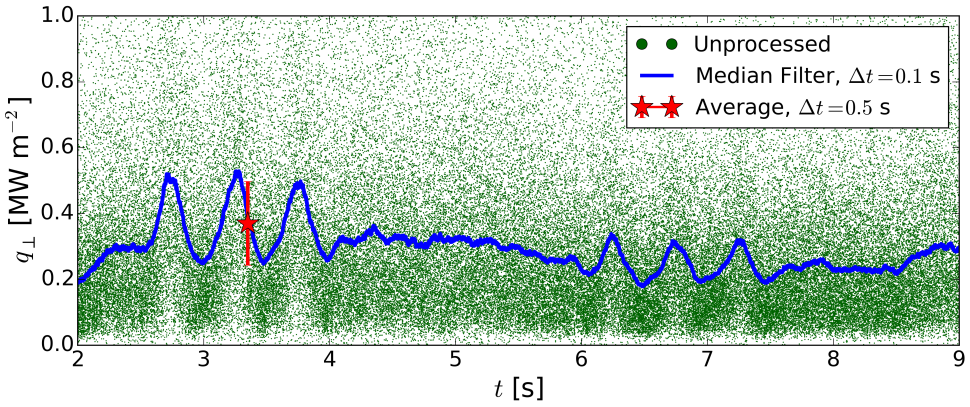

Figure 9: Signal processing of the $q_\perp$ data measured by a Langmuir probe.

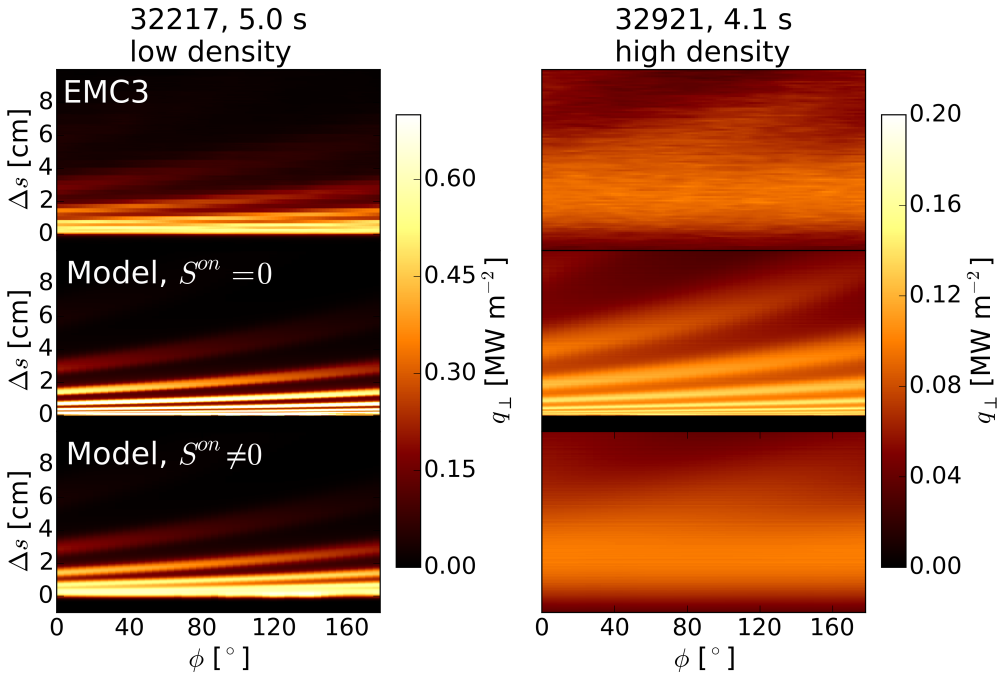

Figure 10: 2D target heat flux patterns for #32217 at 5.0 s (left) and #32922 at 4.1 s (right) obtained by EMC3-EIRENE (top), and an ad-hoc model with the assumption of no divertor spreading (middle), and with divertor spreading (bottom).

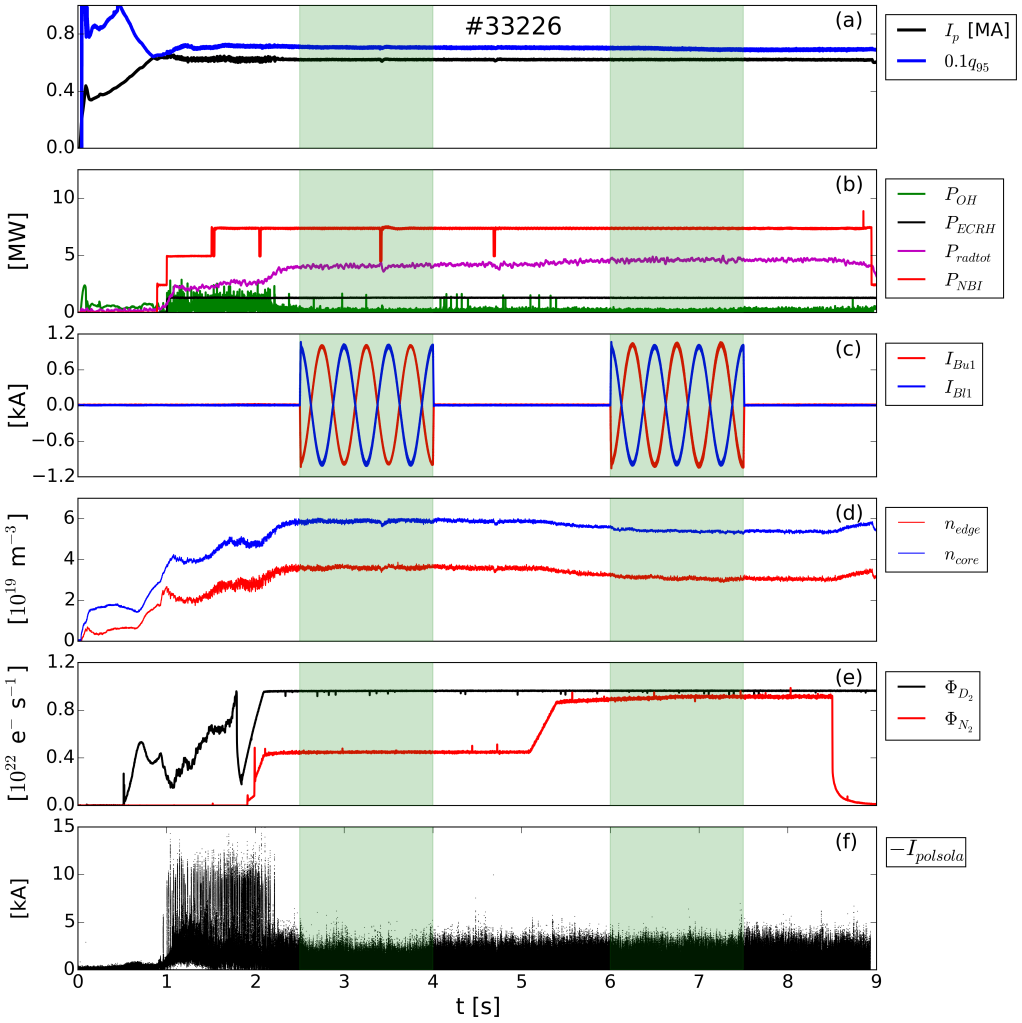

Figure 11: Time traces of plasma current I_p and safety factor q_{95} (a), heating and total radiation (b), coil currents I_{Bu1} and I_{Bl1} (c), line integrated edge and core densities n_{edge} and n_{core} (d), deuterium and nitrogen puff rates Φ_{D2} and Φ_{N2} (e), and divertor shunt current $I_{polsola}$ (f) for the H-mode discharge #33226.

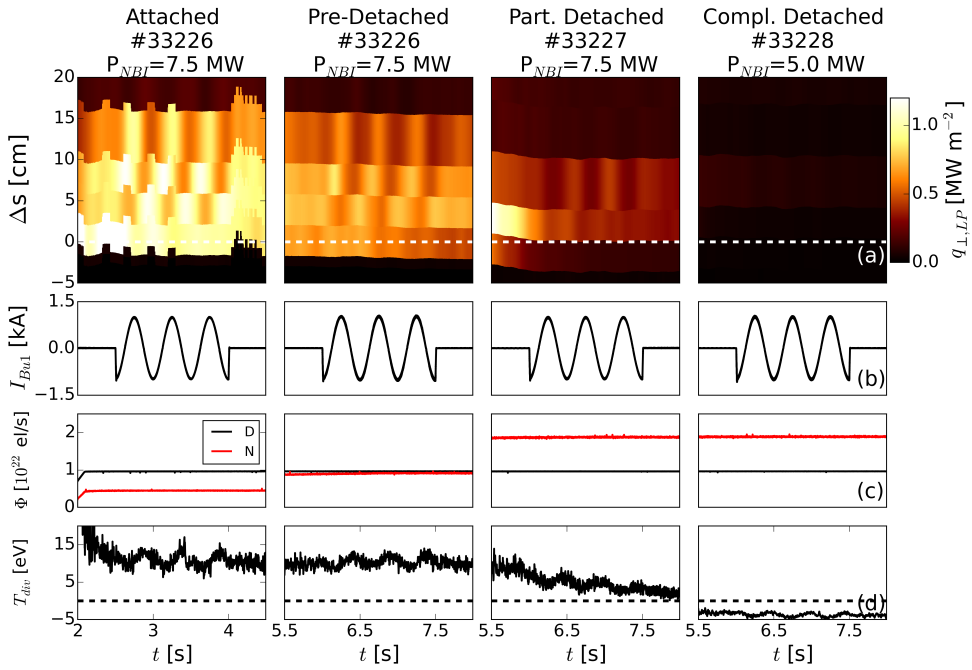

Figure 12: Time traces of the heat flux profile (a) measured by Langmuir probes for time-slices from discharges #33226, #33227 and #33228 with $\Delta\phi = 180°$ and corresponding MP coil current I_{Bu1} (b), nitrogen and deuterium seeding rates Φ_{N2} and Φ_{D2} (c) and T_{div} signal (d).

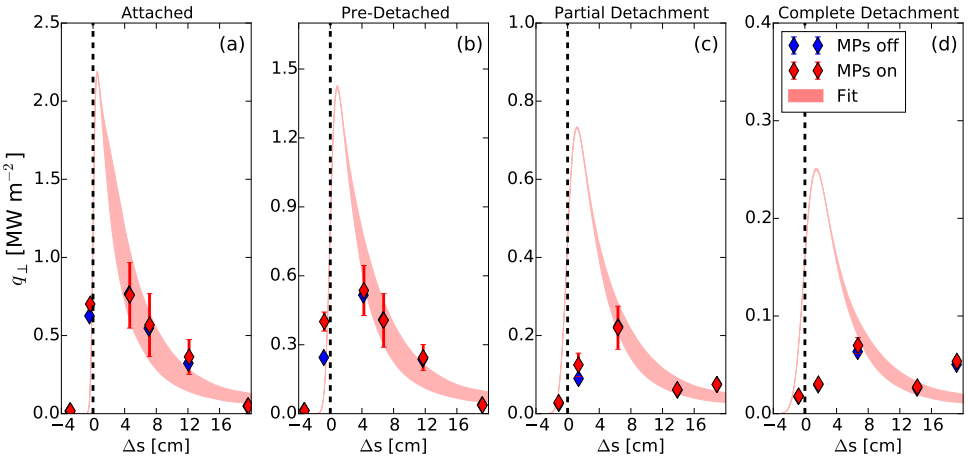

Figure 13: Outer target heat flux profiles for the H-mode discharges #33226, #33227 and #33228 with $\Delta\phi$=180°. The blue symbols correspond to the MP-off values and the red ones to the MP-on values. The error bars show in both cases the measured amplitude of the heat flux variations. The red shaded curves show fits to the MP-on profiles, where the semi-analytical model described in section 2.4 was used. The vertical width of the red shaded region indicates the amplitude of the heat flux variations obtained by the fit.